PHOTONICS Research

2D-to-3D buckling transformability enabled reconfigurable metamaterials for tunable chirality and focusing effect

Donghai Han,[1] Wenkang Li,[1] Tao Sun,[1] Min Liu,[2] Xiaoming Chen,[2] Hongyu Shi,[2] Zhengjie Fan,[1] Fanqi Meng,[3] Liuyang Zhang,[1,*] and Xuefeng Chen[1]

[1]State Key Laboratory for Manufacturing Systems Engineering, Xi'an Jiaotong University, Xi'an 710049, China
[2]School of Information and Communications Engineering, Xi'an Jiaotong University, Xi'an 710049, China
[3]Physikalisches Institut, Goethe-Universität, 60438 Frankfurt am Main, Germany
*Corresponding author: liuyangzhang@xjtu.edu.cn

Received 18 July 2023; revised 9 August 2023; accepted 20 August 2023; posted 21 August 2023 (Doc. ID 500751); published 1 October 2023

Recently, multifarious deformation approaches in nature have promoted dynamic manipulation for electromagnetic (EM) waves in metamaterials, and those representative strategies are mainly focused on the modulation of spectral parameters. Several works have also achieved tunable phase-gradient meta-devices. Here, to broaden the modulation freedom of mechanical deformation, we initially propose two reconfigurable metamaterials consisting of mirrored S-shaped meta-atoms selectively bonded on biaxially pre-stretched substrates. Planar meta-atoms with spin-insensitive transmittance are buckled into 3D morphologies to break residual symmetries by releasing the stress and to facilitate spin-dependent transmittance under circularly polarized incidence. Owing to the geometric anisotropy of S-shaped meta-atoms along the *x* and *y* axes, 3D chiral meta-atoms exhibit discriminate circularly cross-polarized transmittance under opposite spins. The underlying physical mechanism reveals that EM resonance originates from the excitation of electric dipoles and magnetic dipoles, and their cross coupling finally triggers the chiral effects of 3D meta-atoms. By introducing the gradient-phase design that keeps unchanged under various strains, two types of meta-atoms with specified orientations are interleaved to design a double-foci metalens, and its 2D-to-3D morphology transformation shortens the focusing length and facilitates the intensity change of two foci. Our approach in designing reconfigurable EM metamaterials with 2D-to-3D buckling transformability can be further extended toward terahertz even optical wavebands, and it may assist with deriving more applicable multi-functionalities in the aspects of imaging, sensing, and holograms.

https://doi.org/10.1364/PRJ.500751

1. INTRODUCTION

Arbitrary manipulation of electromagnetic (EM) waves has received widespread and long-standing concerns from researchers since the arise of Maxwell's equation. By now, versatile functional components have been developed to operate from the microwave to visible frequency; however, more applicable requirements (e.g., flexibility, tunability, conformability) have arisen to challenge the upper limits of conventional components. As an artificial engineered structure, metamaterial has been widely investigated to manipulate EM waves with extraordinary design flexibility, so as to facilitate numerous functionalities such as vortex beam generation [1,2], multi-foci imaging [3], beam steering [4], and information encoding [5,6]. The majority of existing EM metamaterials belongs to passive structures, and their EM manipulation capabilities cannot be changed once fabricated. Recently, several approaches have emerged using 2D materials [7–9], phase-transition materials [10–12], semimetals [13–15], and active elements [16–18] to achieve the tunability of EM metamaterials by changing the effective physical parameters of internal constituents under external stimulus. Except for the bulk active elements, other tunable pathways are preferably adopted to integrate with submillimeter-scale units at terahertz frequencies. For example, Chen *et al.* [19] have proposed an electrically programmable terahertz metamaterial consisting of 8 × 8 pixels to modulate the amplitude, and a single pixel is composed of 10 × 10 units embedded with vanadium dioxide material. At microwave frequencies, the active elements are incorporated with designed units to encode expected multi-functionalities in the aspects of diffractive deep neural network [20], wireless communication [21,22], orbital angular momentum generation [23], etc. The active material/element-enabled metamaterials indeed provide

reliable platforms to achieve EM multi-functionalities; however, the complicated structural composition and external processing modules face great challenges on the miniaturization.

Recently, the geometric deformation has been demonstrated to play important roles in dynamically engineering EM responses in metamaterials. Among previously engineered reconfigurable metamaterials, origami/kirigami-enabled supportive structures have been extensively adopted to facilitate the in-plane or 2D-to-3D transformation of metamaterial and exhibit dynamic EM responses such as chirality [24,25], toroidal dipolar resonance [26], magnetic polaritons [27], and colorful encryption [28]. Notably, the kirigami reconfiguration mechanism exhibits inimitable advantages not only in modulation capabilities but also in wideband operating frequencies from microwave to optics. For example, a three-layered nano-kirigami metamaterial is reconfigured between 2D and 3D morphology by controlling attractive electrostatic forces between the top gold nanostructure and bottom silicon substrate via applying external voltages, which promotes the chiral reconfiguration and controllable circular dichroism at optical frequencies [29]. Moreover, by arming the meta-atoms with micromotors, mechanically programmable EM metamaterials have been engineered to modulate the reflection phases of meta-atoms by altering the orientations, and various gradient-phase designs can be implemented to achieve multi-functionalities (e.g., arbitrary reflection [30], multiple vortex beam generation, multiple holographic imaging [31]) at microwave frequencies. Despite the versatile functionalities, these programmable metamaterials cannot develop transmissive applications owing to the wave prohibition of bulk motors, and it is also difficult to overcome the fabrication challenges to extend such a mechanism toward terahertz even optics band. Recent advances in flexible electronics have inspired a 2D-to-3D assembly technique to construct versatile 3D structures with micrometer-scale or millimeter-scale size [32–35]. Such a reconfiguration mechanism proposes to transform the 2D precursors selectively bonded on a pre-stretched substrate into 3D morphologies by releasing the substrate stress. In combination with the assembly technique, several reconfigurable EM metamaterials have been proposed to acquire stable microwave frequency selection [36], controllable terahertz chirality [37,38], and tunable optical scattering [39]. Compared with most kirigami-enabled metamaterials usually possessing four resonators in one meta-atom, the assembly-based metamaterial concentrates on the 3D deformation of an individual resonant structure with a large tunable degree of freedom. It should be noted that these above mechanical modulation strategies possess slow responsive speed under the external actuating compared with the electrically tunable metamaterials. However, the mechanical methods possess flexibility, stretchability, and even conformability, which can intrigue functional applications in the aspects of sensing [40] and wearable electronics [41]. For the 2D-to-3D assembly strategy, the versatile deformation modes of the assembly mechanism have large application potential to inspire more prospects for EM multi-functionalities.

In this work, we propose and experimentally demonstrate two novel reconfigurable metamaterials in which the S-shaped meta-atoms can repeatedly transform between 2D and 3D chiral morphologies, which is accompanied with gradient-phase design to enable a double-foci metalens with tunable focusing intensity. Initially, an S-shaped meta-atom array selectively bonded on a biaxially pre-stretched substrate is transformed into 3D chiral morphologies under the stress release, and its transmittance exhibits spin-dependent co- and cross-polarized transmittance components under circularly polarized incidence. The fabricated samples with favorable mechanical flexibility and EM transmittance spectra validate the practicality of the proposed reconfiguration mechanism. The multipolar scattering analysis together with surface current distribution in S-shaped meta-atom indicates that EM resonance originates from the excitation of electric dipoles and magnetic dipoles, and the spin-dependent effects are essentially attributed to cross coupling of these two dipoles. By altering the orientations of meta-atoms, the cross-polarized transmittance phases exhibit a nearly linear increase trend, and the 3D buckling deformation cannot change the robustness of designed gradient-phases. To broaden the dynamic manipulation capabilities of 2D-to-3D buckling transformation in EM metamaterials, meta-atoms with mirrored S-shape are interleaved to construct a transversely double-foci metalens to achieve the tunable focusing length and intensity. These results have validated the feasibility of 2D-to-3D buckling transformation in tunable functional EM metamaterials, and the reconfiguration mechanism supplies new branches for flexible and multifunctional EM meta-devices.

2. MATERIALS AND METHODS

As shown in Fig. 1(a), our proposed reconfigurable metamaterial is composed of periodically arranged S-shaped meta-atoms, which can be transformed together from 2D precursors into 3D morphologies. Specifically, the meta-atoms are attached to a temperature release tape (TRT) sheet to preserve the periodic array, and their circle ends are applied with adhesive to be bonded with biaxially pre-stretched substrate. With the biaxial stress release, all meta-atoms undergo large upward displacement while the selective bonding regions at the circle ends hardly possess z-directional deformation, and the metamaterial is successfully endowed with 2D-to-3D transformability. For our design, the silicone is selected as the constituent material of the substrate, and circularly polarized waves are employed to illuminate the metamaterial in various deformed states. To avoid the plastic deformation during the transforming process, flexible polyimide (PI) is incorporated downward with the copper to construct the S-shaped resonators. Also, the 3D-to-2D deformation of metamaterial can be reversibly achieved by biaxially stretching the hyper-elastic substrate. Here, we have proposed two meta-atoms with mirrored S-shape [classified as A and B shown in Fig. 1(b)] to investigate the effectiveness of the 2D-to-3D buckling reconfiguration mechanism. The periodic constant is $P = 12.6$ mm for the planar metamaterial with the tensile pre-strain $\varepsilon_{\text{pre}} = 40\%$ and evolves into 9 mm as the strain is entirely released. The thicknesses of the free substrate and copper/PI layer are optimized as 2 mm and 12 μm/25 μm, respectively. The other geometric parameters of the meta-atom are as follows: the diameter of the circle ends $d = 2$ mm, the central distance of the ends $l = 7$ mm, the width $w = 0.6$ mm, the inner radius of S-shape $r = 1.46$ mm, and

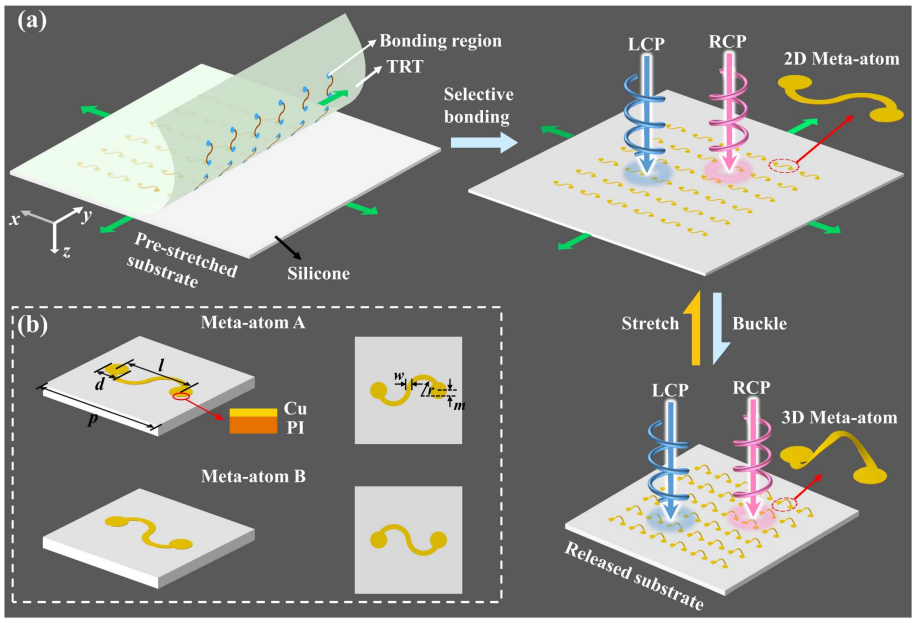

Fig. 1. Schematic illustration of the proposed reconfigurable metamaterial and its constituent meta-atom. (a) 3D reconfiguration mechanism and incidence polarization states of electromagnetic metamaterial. (b) Structural composition and geometrical parameters of the proposed meta-atoms A and B.

the y-directional central distance between circle end and S-shape arc $m = 0.2$ mm.

In such a reconfiguration design, the selective bonding of S-shaped meta-atom determines the 2D-to-3D morphological transformation. To quantitatively investigate mechanical characteristics of the proposed metamaterial, the overall deformation process in Fig. 1(a) is calculated by finite element analysis (FEA) in ABAQUS software. In the calculation, a single meta-atom is representatively considered to simulate the deformation process owing to the metamaterial periodicity. The substrate meshed with hybrid hexahedron elements is first stretched to the strain 40%, and the following deformation stage of the meta-atom is established by importing the meshes and nodal stresses of deformed substrate as initial state. The planar meta-atom is selectively tied on the substrate and finally transformed into 3D morphologies by releasing the substrate pre-strain. The hyper-elastic constitutive relation of silicone material is described by the Mooney–Rivlin model ($C_{10} = -0.1152$ MPa, $C_{01} = 0.8989$ MPa, $D_1 = 0$) according to the tensile test of silicone material. The elastic modulus of the copper and PI is 119 GPa and 2.5 GPa, respectively, and their corresponding Poisson's ratio is 0.34. To verify the morphological reconfiguration modulated EM responses, full-wave simulations are adopted to calculate spectral responses and monitor spatial electric fields in CST software. The deformed morphologies of meta-atoms in ABAQUS are imported into CST to establish the geometric model, and circularly polarized waves are adopted to illuminate the metamaterials toward the z direction. The electric conductivity of the copper is set as 5.96×10^7 S/m, and the complex permittivity of the silicone and PI is $3.1(1 + i0.005)$ and $3.5(1 + i0.0027)$, respectively. To imitate the infinite boundary of metamaterial, the unit cell boundary condition and open boundary condition are applied on the x-o-y plane and along the propagation direction, respectively.

3. RESULTS AND DISCUSSION

Figure 2(a) illustrates the schematic deformation process of single meta-atoms A and B and their FEA simulated stress distributions in deformed states. Initially, the designed planar meta-atoms possess an asymmetry on the x-o-y plane while maintaining the symmetry along the z-direction. When the planar meta-atoms are buckled into 3D morphologies after the stress release, the upward displacement facilitates the breakage of residual symmetries along the z direction to enhance the structural chirality. The 3D chiral meta-atoms A and B are mirrored on the x-o-y plane; in other words, their structural chirality will be opposite. The FEA simulations indicate that the stress is primarily accumulated on the S-shaped arm, and the minor deformation of bonding regions is owed to the 4 orders of magnitude difference between the elastic modulus of copper and silicone. Also, the structural transformation from the chirality to non-chirality is available by stretching the substrate.

The implementation of such a reconfiguration mechanism essentially aims to achieve dynamic EM responses of metamaterials. We have simulated the circularly polarized transmittance components T_{ij}, where the subscript i and j refer to the polarization state of transmitted and incident wave, respectively. Herein, the characters "−" and "+" represent the left- (LCP) and right-circular polarization (RCP), respectively. As shown in Fig. 2(b), the planar metamaterials without chirality possess overlapped co- (T_{--} and T_{++}) and cross-polarized (T_{+-} and T_{-+}) transmittance for both meta-atoms A and B, and there exists a resonance at 8.6 GHz. As the tensile strain 40% is entirely released in metamaterial A, both co- and

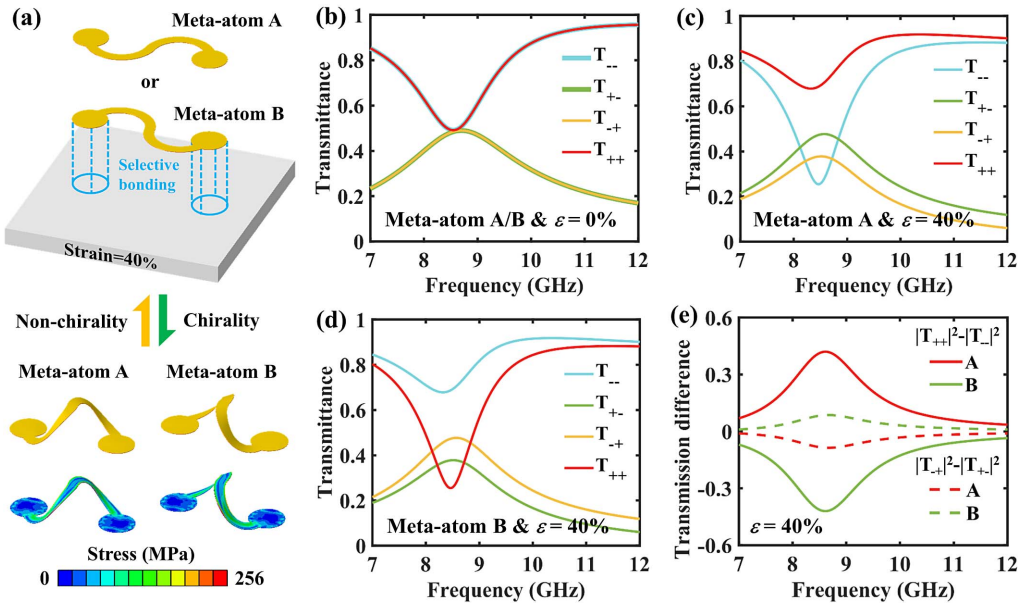

Fig. 2. Simulated deformation and transmittance of the proposed reconfigurable metamaterials. (a) Schematic reconfiguration of meta-atoms and their stress distributions calculated by FEA. Transmittance components of (b) planar metamaterial consisting of meta-atom A or B, and (c), (d) 3D deformed ($\varepsilon = 40\%$) metamaterial consisting of meta-atoms A and B under circularly polarized incidence. (e) Circularly co- and cross-polarized transmittance difference of deformed metamaterials A and B.

cross-polarized components exhibit the transmittance difference between LCP and RCP incidence in Fig. 2(c). For the co-polarized incidence, 3D metamaterial A presents higher resonant amplitudes ($T_{++} = 0.68$) at 8.3 GHz under RCP than that ($T_{--} = 0.26$) at 8.5 GHz under LCP. Compared to these chiral metamaterials merely possessing co-polarized transmittance difference [42,43], T_{+-} and T_{-+} components possess maximum amplitude 0.48 at 8.6 GHz and 0.38 at 8.5 GHz in 3D metamaterial A, respectively. Such a phenomenon should satisfy the condition that the complex co-polarized transmittance must be different under x- and y-polarized incidence (see Appendix B for detailed derivation). For the deformed meta-atom A, the geometric anisotropy along x and y axes determines different linearly co-polarized transmittance amplitude and phase [see Figs. 8(a) and 8(b) in Appendix B]. More importantly, by comparing the profile in Figs. 2(c) and 2(d), it can be observed that the transmittance components of 3D chiral metamaterials A and B exhibit opposite spin-dependent EM responses. To further characterize the spin-dependent transmittance, we have plotted the transmittance difference for co-polarization $|T_{++}|^2 - |T_{--}|^2$ and cross-polarization $|T_{-+}|^2 - |T_{+-}|^2$ in Fig. 2(e), where the profiles for meta-atoms A and B are mirrored. Additionally, the maximum transmittance difference for meta-atom A (or B) can reach 0.42 (or −0.42) under the co-polarization and −0.09 (or 0.09) under the cross-polarization, respectively. The above analysis reveals that 2D-to-3D transformation of the proposed S-shape metamaterials provides a reliable strategy for spin-dependent co- and cross-polarized transmittance.

To verify the practical feasibility of proposed mechanical modulation principle, we have fabricated two reconfigurable chiral metamaterial samples consisting of 22×22 S-shaped meta-atoms. As expected, all meta-atoms are transformed into an ensemble of 3D morphologies, and the overall sample exhibits excellent periodicity, as shown in the left subplot of Fig. 3(a). The fabricated sample also possesses conformal capability to the cylinder surface in the right subplot of Fig. 3(a). Figure 3(b) displays the 2D and 3D metamaterial samples consisting of meta-atoms A and B after several cycles of release and stretching, and the sample still maintains accordance with expected morphologies. To characterize the spectral responses of two samples, a far-field measurement system is adopted to measure the linearly polarized transmittance components that can be transferred to circularly polarized transmittance by the Jones matrix. For the measurement system [Fig. 3(c)], an emitting horn antenna with linear polarization is placed on the top to illuminate the sample, and another linear horn antenna is placed under the sample to receive the transmitted waves. Two antennas are connected to two ports of a vector network analyzer to obtain the transmittance amplitude and phase (see more details in Appendix A).

As shown in Figs. 3(d) and 3(f), two planar samples possess overlapped co- and cross-polarized transmittance curves, and their resonant frequency is around 8.6 GHz, which is in accordance with simulated results. For the co-polarization transmittance of deformed metamaterial A, the resonant amplitude ($T_{++} = 0.66$) at 8.0 GHz under RCP is higher than that ($T_{--} = 0.34$) at 8.3 GHz under LCP, as shown in Fig. 3(e). Compared with simulated result, the frequency deviation ~0.3 GHz and the amplitude deviation ~0.1 are attributed to geometric difference between the FEA simulated structure and fabricated sample. The cross-polarized transmittance difference ($T_{+-} > T_{-+}$) can also be observed for the deformed metamaterial A sample. As mentioned in the simulation

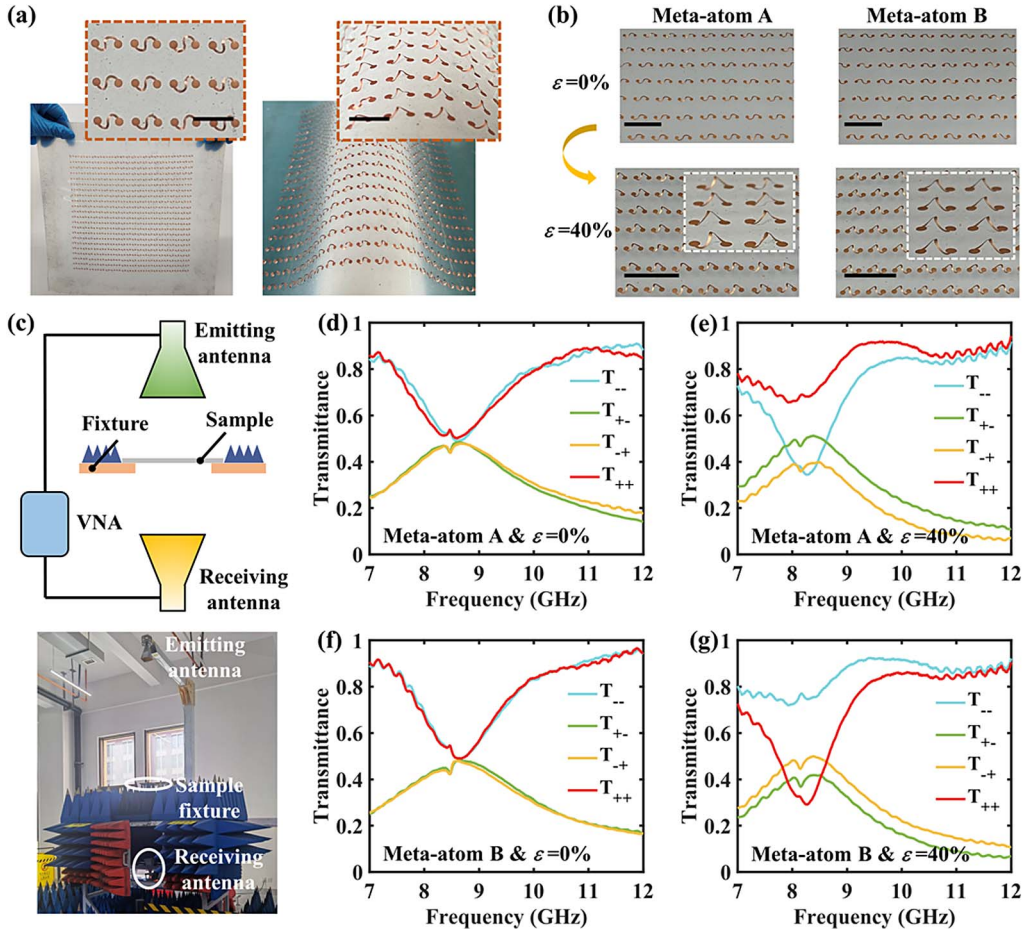

Fig. 3. Fabricated reconfigurable metamaterial samples and their measured transmittance spectra. (a) Fabricated metamaterial sample and its flexible characteristics (scale bars, 9 mm). (b) 2D and 3D morphologies of fabricated samples corresponding to meta-atoms A and B (scale bars, 18 mm). (c) Schematic and physical view of far-field measurement system. Measured transmittance components of metamaterial A in (d) planar state and (e) 3D deformed state, and metamaterial B in (f) planar state and (g) 3D deformed state.

analysis, the opposite spin-dependent transmittance can be observed for another deformed sample in Fig. 3(g). Thus, it can be concluded that reconfigurable metamaterials based on 2D-to-3D buckling are practically feasible to be fabricated and to provide excellent tunability in chiral responses.

For the above simulated and experimental spectra, it is crucial to investigate the physical mechanism to unveil the origination of chiral responses. As shown in Fig. 4(a), the LCP and RCP incident waves excite opposite surface currents accumulated on the S-shaped arm of 3D meta-atom A at 8.5 GHz. The currents on the 3D arm result in the accumulation of the negative and positive electric charges at the circular ends, which facilitates the formation of an electric dipole (red arrow) on the *x-o-y* plane. Meanwhile, two magnetic dipoles (green arrow) are produced with equivalent components on the *x-o-y* plane yet opposite *z* components, and the superposition dipolar vector is located on the *x-o-y* plane. Moreover, the LCP incidence induces strong currents on the 3D S-shaped arm, which means that the LCP wave interacts strongly with the meta-atom, while the current magnitude for RCP incidence is relatively weak. Such a comparison verifies the spin-dependent transmittance spectra of 3D metamaterial A in Fig. 2(c). To further make a quantitative analysis, we have simulated the surface current at frequencies from 7 GHz to 12 GHz with an interval 0.2 GHz and calculated the scattering power of multiple dipoles in 3D meta-atom A under LCP and RCP incidence based on the general multipole scattering theory [44]. Figure 4(b) exhibits the scattering power of electric dipole (*P*), magnetic dipole (*M*), toroidal dipole (TD), and magnetic quadrupole (MQ) and neglects other dipolar components with minor scattering magnitudes. Under the LCP incidence, both the *x* and *y* components of the electric dipole and magnetic dipole dominate the scattering power, which is in accordance with the microscopic characteristics of surface currents. And the scattering power of the *x* component of the electric dipole is nearly 2 orders of magnitude higher than that of the other three dipolar components. By comparison, the total scattering efficiency of 3D meta-atom A under the RCP incidence is lower than that under the LCP incidence, which means that the interaction between the RCP incidence and 3D meta-atom A is weak and, thus, the RCP wave is transmitted with low loss. Essentially, the chiral-optics originates from the cross coupling between electric dipoles and magnetic dipoles [45]. Herein, the non-orthogonal dipole vectors *P* and *M* in 3D meta-atom A can lead to the

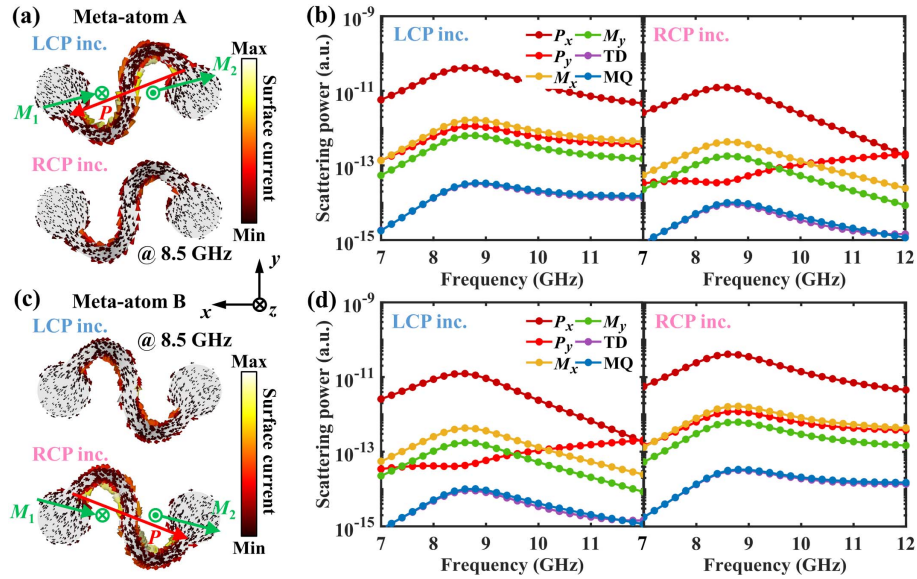

Fig. 4. Physical mechanisms of the spin-dependent transmittance in the deformed meta-atoms. (a) Simulated surface current distributions and (b) calculated scattering power corresponding to electric dipole (P), magnetic dipole (M), toroidal dipole (TD), and magnetic quadrupole (MQ) of 3D meta-atom A under LCP and RCP incidence. (c) Simulated surface current and (d) calculated multipolar scattering power of 3D meta-atom B under LCP and RCP incidence.

chiral responses. Differentially, the intrinsic geometric characteristics of 3D meta-atom B induce the weak interaction with the LCP wave yet strong interaction with RCP, and the current density under LCP is smaller than that under RCP, as shown in Fig. 4(c). There still exists a single electric dipole and two magnetic dipoles in 3D meta-atom B, and their cross coupling effect is also available while the $P \cdot M$ value in 3D meta-atom B is opposite of that in 3D meta-atom A. As for the calculated scattering power of 3D meta-atom B shown in Fig. 4(d), it can be observed that the dominant dipoles possess higher magnitude under RCP than that under LCP, which induces that the LCP wave propagates through 3D meta-atom B with high transmittance. In our proposed metamaterials, the resonance mainly originates from the excitation of electric dipoles and magnetic dipoles, and their cross coupling effect induces the chiral responses in the transmittance spectra.

To further investigate applicability of 2D-to-3D buckling transformability in EM metamaterials, we have proposed a reconfigurable metalens by interleaving geometrical phases of meta-atoms A and B. As schematically depicted in Fig. 5(a), meta-atoms A and B are arranged to focus the LCP incident wave at the location x_1 and x_2, respectively. Before assembling the metalens, cross-polarized transmittance phases are first investigated by altering the orientations α of S-shaped meta-atoms. Herein, we have swept α from 0° to 165° with an interval 15° and plotted the phase in Fig. 5(b). It can be evidently observed that geometrical phases of undeformed meta-atom A exhibit a linearly increasing trend at any frequencies and these gradient-phases are still robust for the deformed meta-atoms. Notably, to design a double-foci metalens with tunable focusing intensity by manipulating T_{+-} amplitude, we take $\alpha = 0°$ as an example to calculate T_{+-} amplitude ratio of meta-atoms A and B in 2D and 3D states. Owing to the lack of chirality, the amplitude ratio of 2D meta-atoms A and B nearly maintains 1 over the overall frequency band [see Fig. 6(a)]. Along the frequency axis, the amplitude ratios of 3D meta-atoms A and B gradually increase while T_{RL} amplitudes evolve into low levels [see Fig. 6(b)]; therefore, the reference frequency is selected as 10 GHz to balance their amplitudes and ratio. Further, we have exhibited T_{+-} amplitude ratio of meta-atoms A and B with various orientations at 10 GHz in Fig. 5(c) and indicate that the amplitude ratio maintains 1 and exceeds 1.45 for any orientations under $\varepsilon = 0\%$ and $\varepsilon = 40\%$, respectively.

With the amplitude and phase analysis of reconfigurable meta-atoms, the metalens is assembled by arranging geometrical phases that are calculated according to

$$\varphi_{i,j} = \frac{2\pi}{\lambda}\left(\sqrt{(x_{i,j} - x_m)^2 + y_{i,j}^2 + f^2} - f\right), \tag{1}$$

where λ is the operating wavelength, the subscripts i and j represent the sequence of meta-atom, and f and x_m ($m = 1, 2$) are the designed focusing length and locations, respectively. In our design, the focusing locations are $x_1 = 50$ mm and $x_2 = -50$ mm, and the focusing length is $f = 200$ mm in the planar metalens. In light of the calculated phase distribution shown in the left subplot of Fig. 5(d), 30 × 30 meta-atoms A and B are interleaved to construct the designed metalens [see right subplot of Fig. 5(d)]. To verify the influence of 2D-to-3D buckling transformation on the controllable focusing characteristics of the metalens, full simulations are adopted to calculate spatial electric fields under the LCP illumination. As shown in Fig. 5(e), the electric field for the 2D metalens indicates that two foci with nearly equivalent intensity are located at $x_1 = 50$ mm and $x_2 = -52$ mm on $z_1 = 200$ mm plane, respectively, which is in great accordance with the design. Based on previous works [46], the substrate release can change the

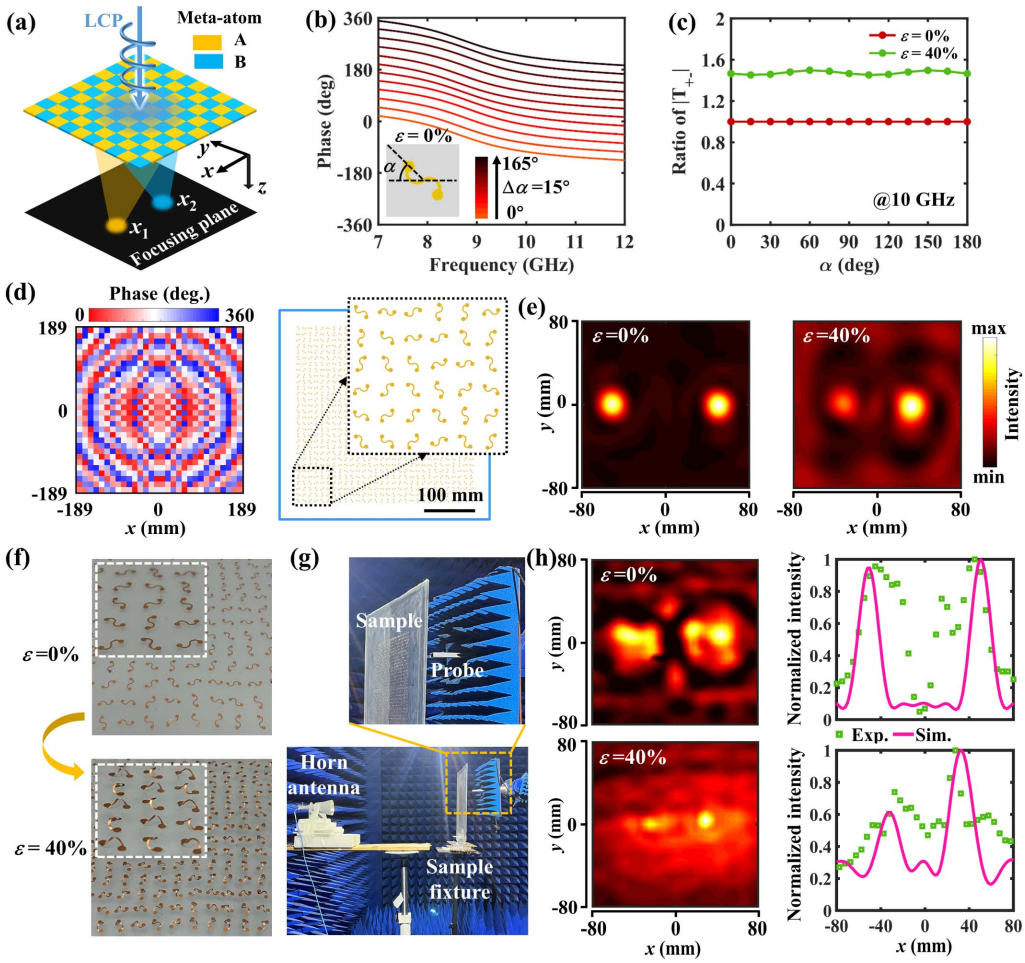

Fig. 5. Design and characterization of a reconfigurable metalens based on 2D-to-3D buckling. (a) Schematic illustration of structural composition and double-foci characteristics of free metalenses. (b) Circularly cross-polarized transmittance phases of undeformed meta-atoms A with various orientations. (c) Transmittance amplitude ratio of meta-atom A and meta-atom B at 10 GHz. (d) Calculated phase distribution on the metalens plane and overall exhibition of designed structure. (e) Full-wave simulated electric field intensity on the focusing plane $z_1 = 200$ mm under $\varepsilon = 0\%$ and $z_2 = 100$ mm under $\varepsilon = 40\%$. (f) 2D and 3D morphology exhibition of fabricated metalens sample. (g) Near-field scanning imaging system for measuring spatial distribution of electric field behind the metalens sample. (h) Measured electric fields and normalized intensity (along $y = 0$ mm) of 2D and 3D metalens.

focusing length from f to $\frac{f}{(1+\varepsilon)^2}$; thus, two foci are exhibited on the focusing plane $z_2 = 100$ mm after releasing the strain $\varepsilon = 40\%$. After the strain release, the focusing locations should be $\frac{x_m}{1+\varepsilon}$ $(m = 1, 2)$, and there exist two foci at $x_1 = 33$ mm and $x_2 = -33$ mm for the simulated field of the 3D metalens. More importantly, the meta-atoms A and B are buckled into 3D morphologies and empowered with high and low cross-polarized transmittance amplitude, respectively; thus, the focusing intensity at x_1 evolves into a higher level than that at x_2. Except for focusing regions, the electric field distribution of the 3D metalens is stronger than that of a 2D one, which is attributed to the high co-polarized amplitudes and low cross-polarized amplitudes in 3D meta-atoms [see Figs. 6(c) and 6(d)]. For practical verification, we have fabricated a metalens sample with its morphology under $\varepsilon = 0\%$ and $\varepsilon = 40\%$ in Fig. 5(f). As shown in Fig. 5(g), the above-mentioned sample is measured by a near-field scanning imaging system in a chamber, where a probe is placed on a robotic arm to detect the transmitted electric field behind the sample with a scanning step 7.5 mm (see Appendix A for more details). The measured electric field is depicted in the left subplots of Fig. 5(h), where two foci of the 2D (or 3D) metalens are located at $x_1 = 42.5$ mm (or 27.5 mm) and $x_2 = -47.5$ mm (or −27.5 mm), respectively. In agreement with simulated results, 3D metalenses also perform with a large difference on the focusing intensity at the locations x_1 and x_2. To further compare the measured and simulated results, the electric field intensity along $y = 0$ mm is normalized to the maximum intensity [see the right subplots of Fig. 5(h)], and focusing locations and bandwidth are marginally deviated, which is originated from the fabrication tolerance and manual measurement deviation. The above results successfully demonstrate the effectiveness of 2D-to-3D buckling on the controllable cross-polarized transmittance difference and extend such spectral responses toward phase-gradient metamaterial design with simultaneous mechanical flexibility and tunable EM focusing

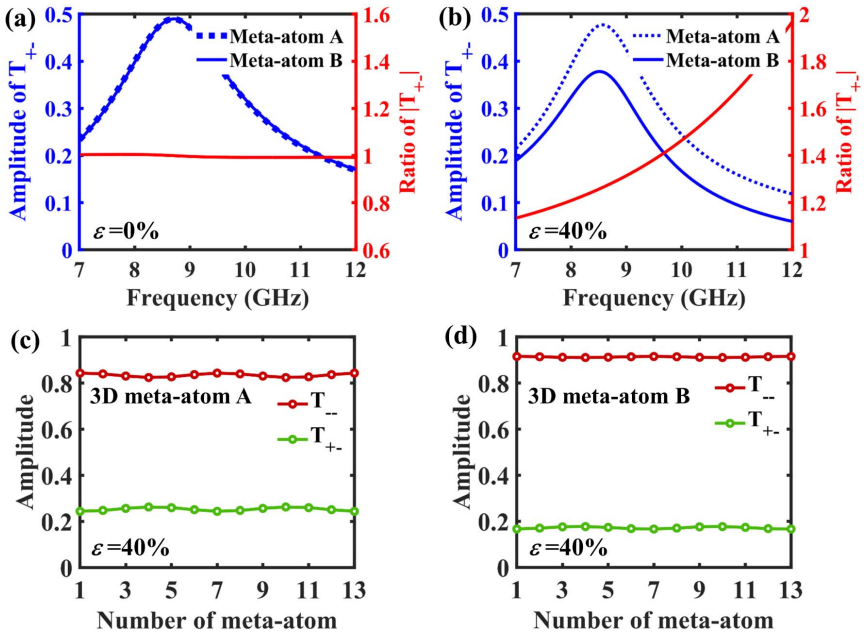

Fig. 6. Circularly cross-polarized transmittance of meta-atom A and B and their amplitude ratio under (a) $\varepsilon = 0\%$ and (b) $\varepsilon = 40\%$. Co- and cross-polarized transmittance amplitude of 3D (a) meta-atom A and (d) meta-atom B.

effects. Moreover, such a 3D buckling deformation strategy is practically feasible and highly efficient to modulate the responses in terahertz and optical metamaterials, where the Ti/SO_2 deposition [37] and the van der Waals forces [39] are utilized to define the selective bonding sites.

4. CONCLUSION

This work has proposed 2D-to-3D buckling-based reconfigurable EM metamaterials, which not only possess mechanical stretchability and flexibility but also can switch spin-dependent co- and cross-polarized transmittance under circularly polarized illumination. Unlike previous origami/kirigami metamaterials where four resonators are necessarily grouped into single meta-atoms, only a single S-shaped resonator can achieve dynamic manipulation for propagated waves in this work. From the perspective of physical mechanism, EM resonance of 3D metamaterials originates from the excitation of electric dipoles and magnetic dipoles, and their cross coupling finally results in the chiral effects of transmittance spectra. By introducing orientation-dependent geometric phases that are robust for 2D/3D meta-atoms, such a reconfiguration method has successfully demonstrated its functionality in the tunable double-foci metalens beyond its dynamic manipulation of spectral responses. The above proposed metamaterials provide several application examples of 2D-to-3D buckling transformation in dynamic manipulation of EM waves, and future investigation with the design of chiral meta-atoms possessing large cross-polarized transmittance difference is promising to achieve metalenses with dynamic foci numbers. The design flexibilities of 2D-to-3D transformable metamaterials can pave new avenues toward reliable applications in EM/optical switching, achromatic imaging, and information processing.

APPENDIX A

1. Fabrication

The fabrication process of the reconfigurable metamaterial primarily utilizes the laser cutting, shadow mask-assisted selective adhering, and thermal transfer technique. As shown in Fig. 7, a bilayer sheet of Cu/PI (12 μm/25 μm) is cut into desired patterns by femtosecond laser ablation (power, 16 W; scanning rate, 0.4 mm/s). Then, a thermal release tape (TRT, release temperature: 90°C–100°C) sheet is laminated onto the cut Cu/PI sheet, and the residual Cu/PI parts are removed from the TRT sheet. A PET mask (0.1 mm thickness) fabricated by carbon dioxide laser ablation is utilized to define the selective regions on the PI side of the S-shaped structures by applying the adhesive (Jule J-527, China). Next, the Cu/PI array together with the TRT layer is laminated (>1 h) on a biaxially stretched silicone substrate. To accelerate the removal of the TRT, it is heated to 300°C. Finally, the planar S-shaped structures are buckled into 3D morphologies under the stress release.

2. Spectral Measurement

Two linearly polarized horn antennas are utilized to radiate EM waves and receive the wave propagating through the metamaterial sample, and two ports of a vector network analyzer (VNA) are connected with two antennas. To support the flexible metamaterial sample, an acrylic plate with 4 mm thickness is utilized, and its transmittance T_{ij}^0 $(i,j = x,y)$ is first measured. By appropriately rotating the sample and the receiving antenna with 90°, the linearly co- and cross-polarized transmittance components can be measured as T_{ij}^1 $(i,j = x,y)$. The transmittance of the sample is finally expressed as $T_{ij} = T_{ij}^1/T_{ij}^0$, which can be transferred to circularly polarized transmittance components via the following equation:

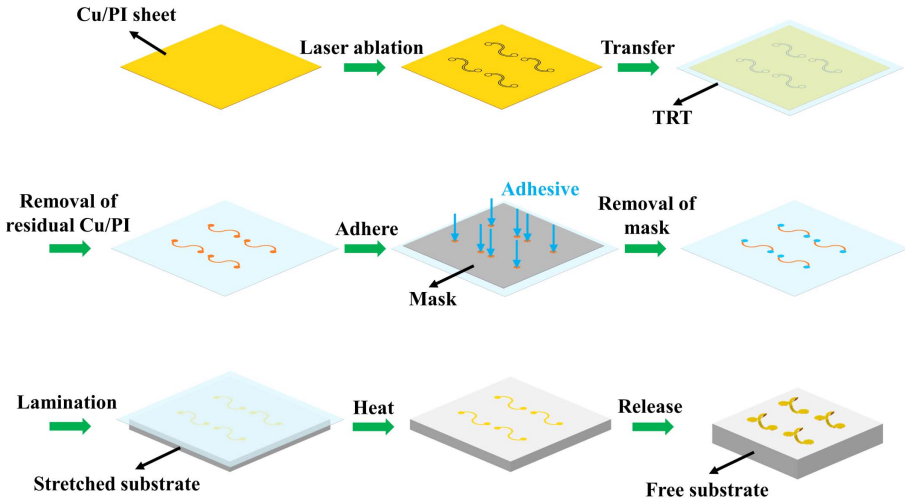

Fig. 7. Fabrication process of 2D-to-3D buckling deformable electromagnetic metamaterials.

$$\begin{pmatrix} T_{++} & T_{-+} \\ T_{+-} & T_{--} \end{pmatrix} = \frac{1}{2}\begin{pmatrix} T_{xx}+T_{yy}+i(T_{xy}-T_{yx}) & T_{xx}-T_{yy}-i(T_{xy}+T_{yx}) \\ T_{xx}-T_{yy}+i(T_{xy}+T_{yx}) & T_{xx}+T_{yy}-i(T_{xy}-T_{yx}) \end{pmatrix}. \tag{A1}$$

3. Electric-field Scanning

The near-field scanning system is utilized to scan the spatial distribution of electric field on the focusing plane of the metalens sample. The fabricated flexible metalens is also placed on the acrylic plate (4 mm thickness) to be fixed with sample stage. In this system, a circularly polarized horn antenna for emitting EM wave is placed with 1 m before the sample fixture, and the transmitted electric-field is detected with the scanning step 7.5 mm by a probe behind the sample. Finally, the measured x (E_x) and y directional (E_y) electric fields are utilized to identify the overall field intensity $|E_x|^2 + |E_y|^2$.

APPENDIX B: GEOMETRIC ANISOTROPY INDUCED CIRCULARLY CROSS-POLARIZED TRANSMITTANCE DIFFERENCE

According to the Eq. (A1), the circularly cross-polarized transmittance difference can be expressed as

$$|T_{-+}|^2 - |T_{+-}|^2 = [\mathrm{Re}(T_{xx}) - \mathrm{Re}(T_{yy})][\mathrm{Im}(T_{xy}) + \mathrm{Im}(T_{yx})] - [\mathrm{Im}(T_{xx}) - \mathrm{Im}(T_{yy})][\mathrm{Re}(T_{xy}) + \mathrm{Re}(T_{yx})], \tag{B1}$$

where the $\mathrm{Re}(T_{ij})$ and $\mathrm{Im}(T_{ij})$ are the real and imaginary parts of the complex transmittance T_{ij}, respectively. It indicates that $|T_{-+}|^2 - |T_{+-}|^2 \neq 0$ requires the condition $T_{xx} \neq T_{xx}$ for a meta-atom; in other words, the meta-atom should possess various characteristics along the x and y directions. As shown in Fig. 8, neither the amplitude nor phase of 3D metamaterial A (or B) is overlapped for T_{xx} and T_{yy}, which can induce the circularly cross-polarized transmittance difference.

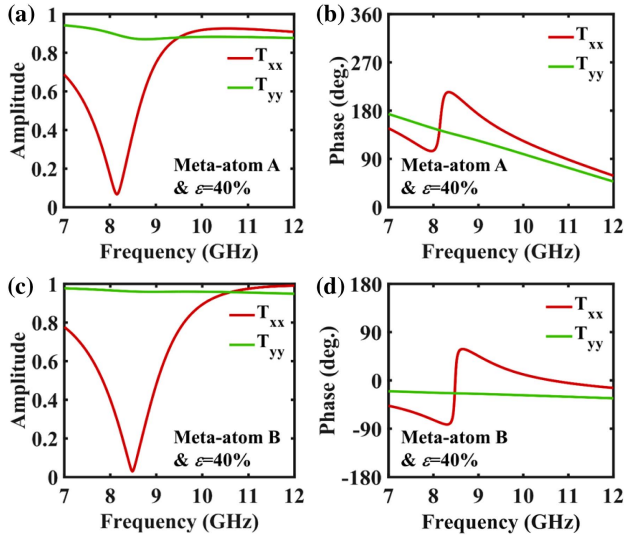

Fig. 8. (a) Amplitude and (b) phase of 3D buckled metamaterial A of the co- and cross-polarized transmittance under x-polarized incidence. (c) Amplitude and (d) phase of 3D metamaterial B of the co- and cross-polarized transmittance under y-polarized incidence.

Funding. National Natural Science Foundation of China (52175115).

Acknowledgment. Liuyang Zhang thanks the National Natural Science Foundation of China for help identifying collaborators for this work.

Disclosures. The authors declare no conflicts of interest.

Data Availability. Data underlying the results presented in this paper are not publicly available at this time but may be obtained from the authors upon reasonable request.

REFERENCES

1. X. Zhang, L. Huang, R. Zhao, Q. Wei, X. Li, G. Geng, J. Li, X. Li, Y. Wang, and S. Zhang, "Multiplexed generation of generalized vortex

beams with on-demand intensity profiles based on metasurfaces," Laser Photon. Rev. **16**, 2100451 (2022).
2. Y. Bao, J. Ni, and C.-W. Qiu, "A minimalist single-layer metasurface for arbitrary and full control of vector vortex beams," Adv. Mater. **32**, 1905659 (2020).
3. X. Zang, H. Ding, Y. Intaravanne, L. Chen, Y. Peng, J. Xie, Q. Ke, A. V. Balakin, A. P. Shkurinov, X. Chen, Y. Zhu, and S. Zhuang, "A multi-foci metalens with polarization-rotated focal points," Laser Photon. Rev. **13**, 1900182 (2019).
4. Y. Yuan, K. Zhang, B. Ratni, Q. Song, X. Ding, Q. Wu, S. N. Burokur, and P. Genevet, "Independent phase modulation for quadruplex polarization channels enabled by chirality-assisted geometric-phase metasurfaces," Nat. Commun. **11**, 4186 (2020).
5. T. Wu, Q. Xu, X. Q. Zhang, Y. H. Xu, X. Y. Chen, X. Feng, L. Niu, F. Huang, J. G. Han, and W. L. Zhang, "Spin-decoupled interference metasurfaces for complete complex-vectorial-field control and five-channel imaging," Adv. Sci. **9**, 2204664 (2022).
6. P. Georgi, Q. Wei, B. Sain, C. Schlickriede, Y. Wang, L. Huang, and T. Zentgraf, "Optical secret sharing with cascaded metasurface holography," Sci. Adv. **7**, eabf9718 (2021).
7. O. Balci, N. Kakenov, E. Karademir, S. Balci, S. Cakmakyapan, E. O. Polat, H. Caglayan, E. Ozbay, and C. Kocabas, "Electrically switchable metadevices via graphene," Sci. Adv. **4**, eaao1749 (2018).
8. J. Zhang, Z. Li, L. Shao, and W. Zhu, "Dynamical absorption manipulation in a graphene-based optically transparent and flexible metasurface," Carbon **176**, 374–382 (2021).
9. Y. Hu, M. Tong, Z. Xu, X. Cheng, and T. Jiang, "Bifunctional spatiotemporal metasurfaces for incident angle-tunable and ultrafast optically switchable electromagnetically induced transparency," Small **17**, 2006489 (2021).
10. M. Liu, E. Plum, H. Li, S. Li, Q. Xu, X. Zhang, C. Zhang, C. Zou, B. Jin, J. Han, and W. Zhang, "Temperature-controlled optical activity and negative refractive index," Adv. Funct. Mater. **31**, 2010249 (2021).
11. Y. Wang, P. Landreman, D. Schoen, K. Okabe, A. Marshall, U. Celano, H. S. P. Wong, J. Park, and M. L. Brongersma, "Electrical tuning of phase-change antennas and metasurfaces," Nat. Nanotechnol. **16**, 667–672 (2021).
12. E. Mikheeva, C. Kyrou, F. Bentata, S. Khadir, S. Cueff, and P. Genevet, "Space and time modulations of light with metasurfaces: recent progress and future prospects," ACS Photon. **9**, 1458–1482 (2022).
13. Y. Cheng, W. Cao, G. Wang, X. He, F. Lin, and F. Liu, "3D Dirac semimetal supported thermal tunable terahertz hybrid plasmonic waveguides," Opt. Express **31**, 17201–17214 (2023).
14. G. Wang, W. Cao, and X. He, "3D Dirac semimetal elliptical fiber supported THz tunable hybrid plasmonic waveguides," IEEE J. Sel. Top. Quantum Electron. **29**, 8400207 (2023).
15. X. He, F. Lin, F. Liu, and W. Shi, "3D Dirac semimetals supported tunable terahertz BIC metamaterials," Nanophotonics **11**, 4705–4714 (2022).
16. S. Venkatesh, X. Lu, H. Saeidi, and K. Sengupta, "A high-speed programmable and scalable terahertz holographic metasurface based on tiled CMOS chips," Nat. Electron. **3**, 785–793 (2020).
17. X. G. Zhang, Q. Yu, W. X. Jiang, Y. L. Sun, L. Bai, Q. Wang, C.-W. Qiu, and T. J. Cui, "Polarization-controlled dual-programmable metasurfaces," Adv. Sci. **7**, 1903382 (2020).
18. L. Zhang, X. Q. Chen, R. W. Shao, J. Y. Dai, Q. Cheng, G. Castaldi, V. Galdi, and T. J. Cui, "Breaking reciprocity with space-time-coding digital metasurfaces," Adv. Mater. **31**, 1904069 (2019).
19. B. Chen, J. Wu, W. Li, C. Zhang, K. Fan, Q. Xue, Y. Chi, Q. Wen, B. Jin, J. Chen, and P. Wu, "Programmable terahertz metamaterials with non-volatile memory," Laser Photon. Rev. **16**, 2100472 (2022).
20. C. Liu, Q. Ma, Z. J. Luo, Q. R. Hong, Q. Xiao, H. C. Zhang, L. Miao, W. M. Yu, Q. Cheng, L. Li, and T. J. Cui, "A programmable diffractive deep neural network based on a digital-coding metasurface array," Nat. Electron. **5**, 113–122 (2022).
21. J. C. Ke, X. Chen, W. Tang, M. Z. Chen, L. Zhang, L. Wang, J. Y. Dai, J. Yang, J. W. Zhang, L. Wu, Q. Cheng, S. Jin, and T. J. Cui, "Space-frequency-polarization-division multiplexed wireless communication system using anisotropic space-time-coding digital metasurface," Nat. Sci. Rev. **9**, nwac225 (2022).
22. C. X. Huang, J. Zhang, Q. Cheng, and T. J. Cui, "Polarization modulation for wireless communications based on metasurfaces," Adv. Funct. Mater. **31**, 2103379 (2021).
23. X. Bai, F. Kong, Y. Sun, G. Wang, J. Qian, X. Li, A. Cao, C. He, X. Liang, R. Jin, and W. Zhu, "High-efficiency transmissive programmable metasurface for multimode OAM generation," Adv. Opt. Mater. **8**, 2000570 (2020).
24. R. Phon, H. Jeong, and S. Lim, "Rotational Kirigami tessellation metasurface for tunable chirality," Adv. Mater. Technol. **7**, 2101706 (2022).
25. W. J. Choi, G. Cheng, Z. Huang, S. Zhang, T. B. Norris, and N. A. Kotov, "Terahertz circular dichroism spectroscopy of biomaterials enabled by kirigami polarization modulators," Nat. Mater. **18**, 820–826 (2019).
26. C. Chen, K. Kaj, Y. Huang, X. Zhao, R. D. Averitt, and X. Zhang, "Tunable toroidal response in a reconfigurable terahertz metamaterial," Adv. Opt. Mater. **9**, 2101215 (2021).
27. M. Li, G. Hu, X. Chen, C.-W. Qiu, H. Chen, and Z. Wang, "Topologically reconfigurable magnetic polaritons," Sci. Adv. **8**, eadd6660 (2022).
28. X. Hou, F. Vogelbacher, X. Lai, K. Li, Y. Song, and M. Li, "Bioinspired multichannel colorful encryption through kirigami activating grating," Sci. Bull. **68**, 276–283 (2023).
29. S. Chen, Z. Liu, H. Du, C. Tang, C.-Y. Ji, B. Quan, R. Pan, L. Yang, X. Li, C. Gu, X. Zhang, Y. Yao, J. Li, N. X. Fang, and J. Li, "Electromechanically reconfigurable optical nano-kirigami," Nat. Commun. **12**, 1299 (2021).
30. W. Yang, K. Chen, Y. Zheng, W. Zhao, Q. Hu, K. Qu, T. Jiang, J. Zhao, and Y. Feng, "Angular-adaptive reconfigurable spin-locked metasurface retroreflector," Adv. Sci. **8**, 2100885 (2021).
31. Q. Xu, X. Su, X. Zhang, L. Dong, L. Liu, Y. Shi, Q. Wang, M. Kang, A. Alù, S. Zhang, J. Han, and W. Zhang, "Mechanically reprogrammable Pancharatnam–Berry metasurface for microwaves," Adv. Photon. **4**, 016002 (2022).
32. Z. Xue, T. Jin, S. Xu, K. Bai, Q. He, F. Zhang, X. Cheng, Z. Ji, W. Pang, Z. Shen, H. Song, Y. Shuai, and Y. Zhang, "Assembly of complex 3D structures and electronics on curved surfaces," Sci. Adv. **8**, eabm6922 (2022).
33. Y. Shuai, J. Zhao, R. Bo, Y. Lan, Z. Lv, and Y. Zhang, "A wrinkling-assisted strategy for controlled interface delamination in mechanically-guided 3D assembly," J. Mech. Phys. Solids **173**, 105203 (2023).
34. Y. Park, H. Luan, K. Kwon, S. Zhao, D. Franklin, H. Wang, H. Zhao, W. Bai, J. U. Kim, W. Lu, J.-H. Kim, Y. Huang, Y. Zhang, and J. A. Rogers, "Transformable, freestanding 3D mesostructures based on transient materials and mechanical interlocking," Adv. Funct. Mater. **29**, 1903181 (2019).
35. Y. Ling, W. Pang, J. Liu, M. Page, Y. Xu, G. Zhao, D. Stalla, J. Xie, Y. Zhang, and Z. Yan, "Bioinspired elastomer composites with programmed mechanical and electrical anisotropies," Nat. Commun. **13**, 524 (2022).
36. X. Fan, Z. Pan, S. Chen, Y. Li, Z. Zhao, and T. Pan, "3D flexible frequency selective surface with stable electromagnetic transmission properties," Adv. Mater. Technol. **7**, 2101316 (2022).
37. H. Zhao, K. Li, M. Han, F. Zhu, A. Vázquez-Guardado, P. Guo, Z. Xie, Y. Park, L. Chen, X. Wang, H. Luan, Y. Yang, H. Wang, C. Liang, Y. Xue, R. D. Schaller, D. Chanda, Y. Huang, Y. Zhang, and J. A. Rogers, "Buckling and twisting of advanced materials into morphable 3D mesostructures," Proc. Natl. Acad. Sci. USA **116**, 13239–13248 (2019).
38. D. Han, X. Fang, L. Zhang, and X. Chen, "Tunable chiral responses in mechanically reconfigurable three-dimensional metamaterials," New J. Phys. **23**, 053001 (2021).
39. W. Liu, Q. Zou, C. Zheng, and C. Jin, "Metal-assisted transfer strategy for construction of 2D and 3D nanostructures on an elastic substrate," ACS Nano **13**, 440–448 (2019).
40. Z. A. Dijvejin, K. K. Kazemi, K. A. Zarasvand, M. H. Zarifi, and K. Golovin, "Kirigami-enabled microwave resonator arrays for wireless, flexible, passive strain sensing," ACS Appl. Mater. Interfaces **12**, 44256–44264 (2020).
41. B.-Y. Yu, D.-W. Yue, K.-X. Hou, L. Ju, H. Chen, C. Ding, Z.-G. Liu, Y.-Q. Dai, H. K. Bisoyi, Y.-S. Guan, W.-B. Lu, C.-H. Li, and Q. Li,

"Stretchable and self-healable spoof plasmonic meta-waveguide for wearable wireless communication system," Light Sci. Appl. **11**, 307 (2022).
42. Z. Wang, L. Jing, K. Yao, Y. Yang, B. Zheng, C. M. Soukoulis, H. Chen, and Y. Liu, "Origami-based reconfigurable metamaterials for tunable chirality," Adv. Mater. **29**, 1700412 (2017).
43. L. Jing, Z. Wang, B. Zheng, H. Wang, Y. Yang, L. Shen, W. Yin, E. Li, and H. Chen, "Kirigami metamaterials for reconfigurable toroidal circular dichroism," NPG Asia Mater. **10**, 888–898 (2018).
44. T. Kaelberer, V. A. Fedotov, N. Papasimakis, D. P. Tsai, and N. I. Zheludev, "Toroidal dipolar response in a metamaterial," Science **330**, 1510–1512 (2010).
45. L. Rosenfeld, "Quantenmechanische Theorie der natürlichen optischen Aktivität von Flüssigkeiten und Gasen," Z. Phys. **52**, 161–174 (1929).
46. A. She, S. Zhang, S. Shian, D. R. Clarke, and F. Capasso, "Adaptive metalenses with simultaneous electrical control of focal length, astigmatism, and shift," Sci. Adv. **4**, eaap9957 (2018).